

# Viscoelastic Capillary Flow Cytometry

Murat Serhatlioglu,\* Emil Alstrup Jensen, Maria Niora, Anne Todsén Hansen, Christian Friberg Nielsen, Michelle Maria Theresia Jansman, Leticia Hosta-Rigau, Morten Hanefeld Dziegiel, Kirstine Berg-Sørensen, Ian David Hickson, and Anders Kristensen\*

A compact microfluidic flow cytometer is demonstrated, comprising viscoelastic flow focusing in fused silica capillaries and a fiber optical interface. Viscoelastic flow focusing enables simple device design and operation with a single-inlet/outlet fluidic configuration. Fused silica capillaries with different inner diameters are effortlessly interchanged to eliminate blockage ratio limitations and enable single-train particle focusing for a wide range of particle sizes and geometries. The compact system is mounted on an inverted microscope for easy integration with optical imaging and other optofluidic modalities, such as optical trapping and particle sorting. A real-time cytometric analysis of three channels, forward scattering, side scattering, and fluorescence detection, is performed on LABVIEW. A throughput of 3500 events  $s^{-1}$  is performed on particles of sizes ranging from 2 to 20  $\mu m$ , using capillaries of different inner diameters ranging from 30 to 75  $\mu m$ . The outer diameter of all capillaries is identical to the cladding diameter of the applied optical fibers. This enables easy exchange and precise optical alignment of fibers and capillaries on a microfabricated jig. The performance of the microfluidic flow cytometer is benchmarked using polystyrene calibration beads, poly(lactic-co-glycolic acid) particles, erythrocytes, THP-1 leukemic monocytes, and human metaphase chromosomes.

In a conventional flow cytometry setup, the particles of interest pass through an optical detection region where the particles interact with one or more laser beams. Scattered laser light from the particle is collected, detected, and simultaneously analyzed to acquire information about the sample. Forward scattered light (FSC) is collected at smaller light scattering angles ( $5^{\circ}$ – $20^{\circ}$ ), giving information about the cell geometry and size, while side scattered light (SSC) is collected at wider angles ( $15^{\circ}$ – $120^{\circ}$ ), giving information about the cell interiors, such as granularity and complexity. Fluorescent labeling for specific biomarkers can also be detected with customized optical filters for fluorescent detection (FL) to derive more detailed chemical and biological information on the targeted particles.


Conventional flow cytometers are complex instruments, where precise assembly and alignment of discrete optical elements and fluidic components imply high acquisition cost and a need for regular maintenance. Integration of microfluidics and

fiber optical elements enables cost-efficient, compact, and robust assembly of flow cytometers. Further, microfluidic flow cytometers (MFC) can analyze smaller volumes of samples. Microfluidic flow cytometry studies are referenced in multiple names such as microflow cytometry, microfluidic flow cytometry, or microfluidic flow cytometer (all abbreviated here as MFC). The field is reviewed in several papers.<sup>[2–6]</sup> Multiple

## 1. Introduction

Since the first demonstration by Wolfgang Gohde in the late 1960s,<sup>[1]</sup> flow cytometry has developed to be a widely used technique with the ability to provide detailed biological characteristics with single-cell resolution. Today, flow cytometry is routinely used in both research, clinical analysis, and in the food industry.

M. Serhatlioglu, E. A. Jensen, M. Niora, M. M. T. Jansman, L. Hosta-Rigau, K. Berg-Sørensen, A. Kristensen  
Department of Health Technology  
Technical University of Denmark  
Ørsted's Plads, Building 345C, 2800 Kongens Lyngby, Denmark  
E-mail: murse@dtu.dk; akri@dtu.dk

 The ORCID identification number(s) for the author(s) of this article can be found under <https://doi.org/10.1002/anbr.202200137>.

© 2022 The Authors. Advanced NanoBiomed Research published by Wiley-VCH GmbH. This is an open access article under the terms of the Creative Commons Attribution License, which permits use, distribution and reproduction in any medium, provided the original work is properly cited.

DOI: 10.1002/anbr.202200137

A. T. Hansen, M. H. Dziegiel  
Department of Clinical Immunology  
University of Copenhagen  
Blegdamsvej 9, 2100 København Ø, Denmark

C. F. Nielsen, I. D. Hickson  
Center for Chromosome Stability  
Department of Cellular and Molecular Medicine  
University of Copenhagen  
2200 København N., Denmark

M. H. Dziegiel  
Department of Clinical Medicine  
University of Copenhagen  
Blegdamsvej 3B, 2200 København N., Denmark

factors should be considered while building a miniaturized optical MFC platforms: substrate material, fluidic and optics integration, and flow focusing method.

Polymer-, silicon-, and glass-based materials are used as the device substrate in MFC platforms.<sup>[7–23]</sup> Polymer-based materials poly(dimethylsiloxane), poly(methyl acrylate), polycarbonate, etc. are advantageous due to their mass production and 3D printer compatibilities; however, they are disadvantageous due to their chemical instability, pressure vulnerability, and autofluorescence. Silicon substrates are compatible with a wide range of planar fabrication techniques; however, their lack of transparency in the visible range is a drawback for optical and fluidic assemblies. Glass materials, specially fused silica (or quartz), on the other hand, are chemically inert, optically transparent in the visible and NIR range, and highly compatible for reusable MFC instrumentation. However, glass machining is a hurdle and requires highly sophisticated tools<sup>[24]</sup> for high-precision glass micromachining.<sup>[19]</sup> Thanks to their abundant availability, fused silica capillaries circumvent the need for expensive and complex fabrication techniques if they are considered as a flow cell for MFC platforms.<sup>[20,21,25]</sup>

Various methods have been implemented in MFC platforms to integrate the fluidic and optical units for efficient optical interaction with the particles of interest. High accuracy, as quantified by the percentage of the coefficient of variation of the measured signal (CV%), requires precise optical alignment of the detection region and the particle trajectory. To this end, inscribed optical waveguides,<sup>[14,26]</sup> micro-optics,<sup>[7,27–32]</sup> and optical fibers<sup>[17,19–21,33,34]</sup> are implemented in MFC platforms. Inscribed waveguides require extra coupling efforts to external lasers and detectors, thus suffering from low coupling efficiency and high-alignment dependency. Microfabricated, integrated optics with on-chip lens systems such as SU-8 microlenses,<sup>[35]</sup> laser beam-shaping prisms,<sup>[36]</sup> and fiber-tipped lenses<sup>[37,38]</sup> have also been applied. The fabricated micro-optics increase the efficiency of light excitation and collection; however, they may introduce another level of complexity at optical alignment accuracy. To prevent that, optical fibers can be inserted through microgrooves that are carefully designed and fabricated to match the outer diameter (OD) of the optical fibers. The inserted fibers are then fixed with an index matching glue to make the system robust. Thus, among all other approaches, bare optical fiber insertion directly to the flow cell avoids free-space optics and provides the most straightforward configuration without sacrificing beam quality and signal detection sensitivity. However, inserting fibers are prone to user-dependent errors; thus, a modular system with interchangeable/replaceable units has prominent advantages in reaching a high degree of robustness.<sup>[39,40]</sup>

Stable and precise particle focusing along the fluid flow axis is essential to obtain high repeatability for the detected signals. The hydrodynamic flow focusing method requires squeezing the sample stream by extensional sheath flow inlets (in 1D or 2D confinement) to the flow axis. Even though it is the most favored method for commercial flow cytometry instruments, it suffers from the need to use multiple pumping channels for more than one inlet. Externally applied actuation forces such as electric,<sup>[41–43]</sup> magnetic,<sup>[44–47]</sup> and acoustic<sup>[48,49]</sup> forces have also been applied in MFC devices. However, such strategies require external sources, i.e., additional complexity.

Nonlinear and tunable flow-focusing methods, such as inertial and viscoelastic focusing techniques, can provide a single train of particles in flow cells with a single inlet/outlet. However, inertial focusing has multiple particle equilibrium positions and requires flow at high Reynolds number ( $Re$ ),  $Re \gg 1$ .<sup>[50,51]</sup> Complex microfluidic architectures for Dean-drag force solutions may address these challenges but will increase the complexity in design and fabrication.<sup>[52]</sup>

On the other hand, viscoelastic particle focusing has great flexibility by tuning the rheological property of the viscoelastic solution to obtain a single equilibrium position. In addition, it is possible to support central axis viscoelastic focusing on a wide range of flow rates ranging from very low  $Re \ll 1$  but also at high  $Re \gg 1$  using a mutual combination of inertial effects in elasto-inertial focusing (in some references inertio-elastic),<sup>[50]</sup> oscillatory flow focusing,<sup>[53]</sup> and using an external electric field in electro-viscoelastic focusing.<sup>[54–57]</sup> Viscoelastic flow-focusing techniques have a high potential for MFC integration. Several studies have demonstrated viscoelastic flow cytometry using optical,<sup>[20,21,37,58]</sup> impedance,<sup>[59,60]</sup> and imaging<sup>[61,62]</sup> detection methods. These studies demonstrated successful cytometric measurements using multiple sizes and geometry of polystyrene beads, human cells, and rod-shaped bacterial cells (Table S1, Supporting Information).

Even though the viscoelastic flow focusing method is a promising tool for MFC platforms, viscoelastic fluid elasticity, shear profile (shear thinning/thickening), and blockage ratio will dramatically affect the efficiency of single-line cell focusing. Fluid elasticity and shear profile are fluid rheology-dependent parameters and can be optimized by tuning the fluid's rheological properties, such as viscosity, polymeric concentration, and molecular weight. However, the blockage ratio ( $\beta$ ) depends on the fixed ratio between particle size and characteristic channel length. To reach an efficient single-file particle trajectory,  $\approx 0.1 < \beta$  and  $\approx 0.25 > \beta$  should be satisfied.<sup>[53,62–65]</sup> Therefore, a modular MFC platform with interchangeable/replaceable units independent from fabrication complexities could have prominent advantages in reaching a stable single-file particle trajectory while keeping  $\beta < 0.25$  for large size range of particles.

This study presents a compact microfluidic flow cytometer comprising viscoelastic flow focusing in fused silica capillaries with a fiber optical interface. A fused silica capillary with a circular cross-section serves as a single inlet/outlet flow cell, and optical fibers are used for laser light delivery and scattered light collection. Viscoelastic flow focusing is optimized to focus different sizes and shapes of the particles at the capillary axis using capillaries with a different inner diameter (ID). The OD of all capillaries is the same and identical to the cladding diameter of the applied optical fibers. This enables easy exchange and precise optical alignment of fibers and capillaries on a microfabricated jig allowing single-line particle trajectory for a large range of particle sizes and geometries. Various types of synthetic and biological particles such as polystyrene (PS) calibration beads, poly(lactic-co-glycolic acid) (PLGA) particles, erythrocytes, THP-1 leukemic monocytes, and human metaphase chromosomes are analyzed by measuring the FSC, SSC, and FL signals. The performance of the viscoelastic MFC is benchmarked against a commercial flow cytometer, BD Fortessa (Becton, Dickinson and Company, NJ USA). The proposed portable

MFC device benefits from the capillary swapping method to reach high flexibility and versatility to run a wide range of particles ranging from 2 to 20  $\mu\text{m}$  (within the range of this study). The measured %CV values with the PS calibration beads match well with the manufacturing certificate of analysis by showing as low as 2.1% value. To the best of our knowledge, this study uses the largest range of particle types, sizes, and shapes running in a stable and fully integrated viscoelastic flow cytometry platform. The compact MFC platform can be mounted on an inverted microscope for integration with optical imaging and other optofluidic modalities, such as light sheet microscopy,<sup>[66]</sup> high-speed imaging cytometry,<sup>[67–69]</sup> Raman spectroscopy (or cytometry),<sup>[70]</sup> optical trapping,<sup>[71,72]</sup> and particle sorting.<sup>[49,73]</sup>

## 2. Experimental Section

### 2.1. Viscoelastic Buffer Preparation

Viscoelastic hyaluronic acid (HA) (1.6 MDa, Sigma-Aldrich) solutions were prepared at two different concentrations (1000 and 5000 ppm) in Milli-Q (MQ) Water, 1X phosphate buffer saline (PBS) (Sigma-Aldrich), and 1X Gibco FluoroBrite (FB) DMEM (ThermoFisher Scientific), and their shear viscosities were measured using a Discovery Hybrid Rheometer 2 (TA instruments, New Castle, Delaware) with a parallel plate geometry (diameter of 20.0 mm and gap distance of 1.0 mm) as given in Supplementary file S1, Supporting Information. PBS and FB were always at a 1X concentration in viscoelastic HA solutions.

### 2.2. Particle and Cell Suspensions

Spherical PS particles of 2.0, 4.0, and 6.0  $\mu\text{m}$  diameter (ThermoFisher Scientific, Flow Cytometry Size Calibration Kit: F13838) were suspended in 1000 ppm HA viscoelastic solution prepared in 1X FB medium at a concentration of  $4 \times 10^6$  particles  $\text{mL}^{-1}$ .

Spherical fluorescent-labeled PS particles of 2.5, 4.0, and 7.0  $\mu\text{m}$  diameter (Duke Scientific) were suspended in 1000 ppm FB-HA viscoelastic solution at a concentration of  $1 \times 10^6$  particles  $\text{mL}^{-1}$ .

PLGA particles were prepared using the double emulsion solvent evaporation method.<sup>[74]</sup> The primary emulsion was obtained by adding 5 mL PLGA (50:50, Mw 30–60 kDa, Sigma-Aldrich) ( $18 \text{ mg mL}^{-1}$  in dichloromethane, DCM) to 250  $\mu\text{L}$  MQ, followed by sonication on ice (20% power, 40 s, 50% duty cycle) (Q700 sonicator with microprobe, Qsonica). The obtained emulsion was added to 10 mL of 2.5% poly(vinylalcohol) (PVA, Mw 13–23 kDa, Sigma-Aldrich) solution and vortexed for 10 s to obtain the secondary emulsion. This emulsion was stirred overnight to allow for DCM evaporation, followed by washing the resulting PLGA particles in MQ ( $3 \times$ , 3500 g, 5 min) (SL 16R centrifuge, ThermoScientific). The size of the PLGA particles was determined using light microscopy (Inversed IX83 microscope, Olympus) and ImageJ software. Six independent PLGA particle batches were assessed. Within each batch, at least 200 particles in five areas were measured. The polydispersity index (PDI) was furthermore determined as the square of the standard deviation divided by the average particle diameter ( $\text{PDI} = [\sigma/d]$ ).

This resulted in a particle diameter of  $1.9 \pm 0.9 \mu\text{m}$ , with a 0.2 PDI. Microscopy images are given in Supplementary file S2, Supporting Information.

Blood samples were collected in 2 mL EDTA blood tubes from Vacuette (Greiner Bio-One). One milliliter was then transferred to a Nunc tube and centrifuged (Eppendorf, Germany) at 5000 rpm for 3 min. Next, the plasma phase was discarded with a micropipette and replaced with the same volume FB medium. The blood sample was then washed with FB medium twice with the same centrifugation parameters. Finally, 2  $\mu\text{L}$  of precipitated red blood cells (RBCs) was dispensed in 1 mL FB-HA viscoelastic medium.

Metaphase chromosomes were isolated from standard, commercially available cell lines, American Type Culture Collection (ATCC). For the preparation, four 15 cm dishes of HCT116 CDK1as<sup>[75]</sup> H2B-EGFP<sup>[76]</sup> cells were arrested for 16 h by 0.25  $\mu\text{M}$  1NM-PP1 in G2, released into and arrested in, mitosis by 200  $\text{ng mL}^{-1}$  nocodazole treatment for 4 h and collected by mitotic flush-off. Chromosomes were then isolated as described previously for HCT116 cells,<sup>[77]</sup> with the exception that the glycerol step gradient had three layers: 30%, 60%, and 80%, to a final concentration of approximately  $2 \times 10^8$  chromosomes  $\text{mL}^{-1}$ . Finally, 10  $\mu\text{L}$  of chromosomes were dispensed in 200  $\mu\text{L}$  FB-HA (20 times dilution) viscoelastic medium. Microscopy images are given in Supplementary file S3, Supporting Information.

THP-1 monocytes from human acute monocytic leukemia were purchased from American Type Culture Collection (ATCC; TIB-202). The cells were maintained in RPMI 1640 medium, supplemented with 10% fetal bovine serum, 100  $\text{U mL}^{-1}$  penicillin, and 100  $\mu\text{g mL}^{-1}$  streptomycin (all from Biowest), at an incubator of 37  $^{\circ}\text{C}$ , 5%  $\text{CO}_2$ , and 100% humidity. We tested cell viability in two viscoelastic solutions: 1000 ppm of HA in 1) PBS (PBS-HA) or 2) FB (FB-HA). Cells were either live or fixed with 4% paraformaldehyde, they were suspended in either PBS or FB, and were further treated with cell-permeable viability stain calcein-AM (Invitrogen; Exc/Em: 494/517 nm). We then merged 10  $\mu\text{L}$  of PBS- or FB-cell suspension into 500  $\mu\text{L}$  of PBS-HA or FB-HA viscoelastic solutions, respectively. Samples were filtered through Falcon cell strainers of 35  $\mu\text{m}$  mesh (Corning), before analyzing by commercial flow cytometry (BD Biosciences; LSRFortessa) and our MFC platform.

Suspension of cells into viscoelastic solutions may change the cell size and affect cell integrity.<sup>[78]</sup> Therefore, we run cell viability tests THP-1 monocytes suspended in viscoelastic solutions. Microscopy images, cell viability tests, and average cell size measurements of THP-1 monocytes are given in Supplementary file S4–S6, Supporting Information. Images of stained cells suspended in viscoelastic medium (FB-HA) were acquired by wide field microscopy to confirm cells morphology remained intact (Supplementary file S4, Supporting Information). Additional cell viability tests by flow cytometry showed that suspension of live unstained cells in FB-HA had no impact on cell size, as compared to cells suspended in FB, whereas cell suspension in both PBS and PBS-HA caused cell size decrease (Supplementary file S5, Supporting Information). In addition, cellular staining (SS) resulted in cell population reduction for both live and fixed cells (Supplementary file S6, Supporting Information). However, stained cells suspended into PBS-HA were more prone to cell

bursting presumably caused by a difference in homeostatic tension. Both cell size analysis and relative cell count analysis showed that FB-HA was a better choice to preserve cell integrity. Therefore, we used FB-HA viscoelastic medium instead of PBS-HA solution for all the MFC and BD Fortessa experiments.

### 2.3. Experimental Setup

The experimental design and schematic view of the prepared flow cytometry platform are given in **Figure 1**. The flow cytometry platform was assembled from two parts. (I) a CO<sub>2</sub> laser-machined (Epilog Zing, 30 W) poly(methyl methacrylate)

(PMMA) substrate and (II) a microfabricated SU-8 jig for fiber and capillary alignment. The optical fibers and microcapillary were placed and fixed on the laser-machined grooves on the PMMA substrate (Figure 1a,b). Screw bolts were used to hold the fibers and glass capillary in the grooves. Optical fiber connectors were connected to mating sleeves for patch fiber connections to the detectors. Two circular openings are made on the PMMA plate to fit the microscope objective when the platform is placed on the microscope. One opening is reserved for fixing the microfabricated SU-8 jig, and the other is for microscope imaging to monitor particle trajectories closer to the outlet.

Three different ID fused silica glass capillaries with the same OD of  $125 \pm 2 \mu\text{m}$  (TSP030150, TSP050150, TSP075150,

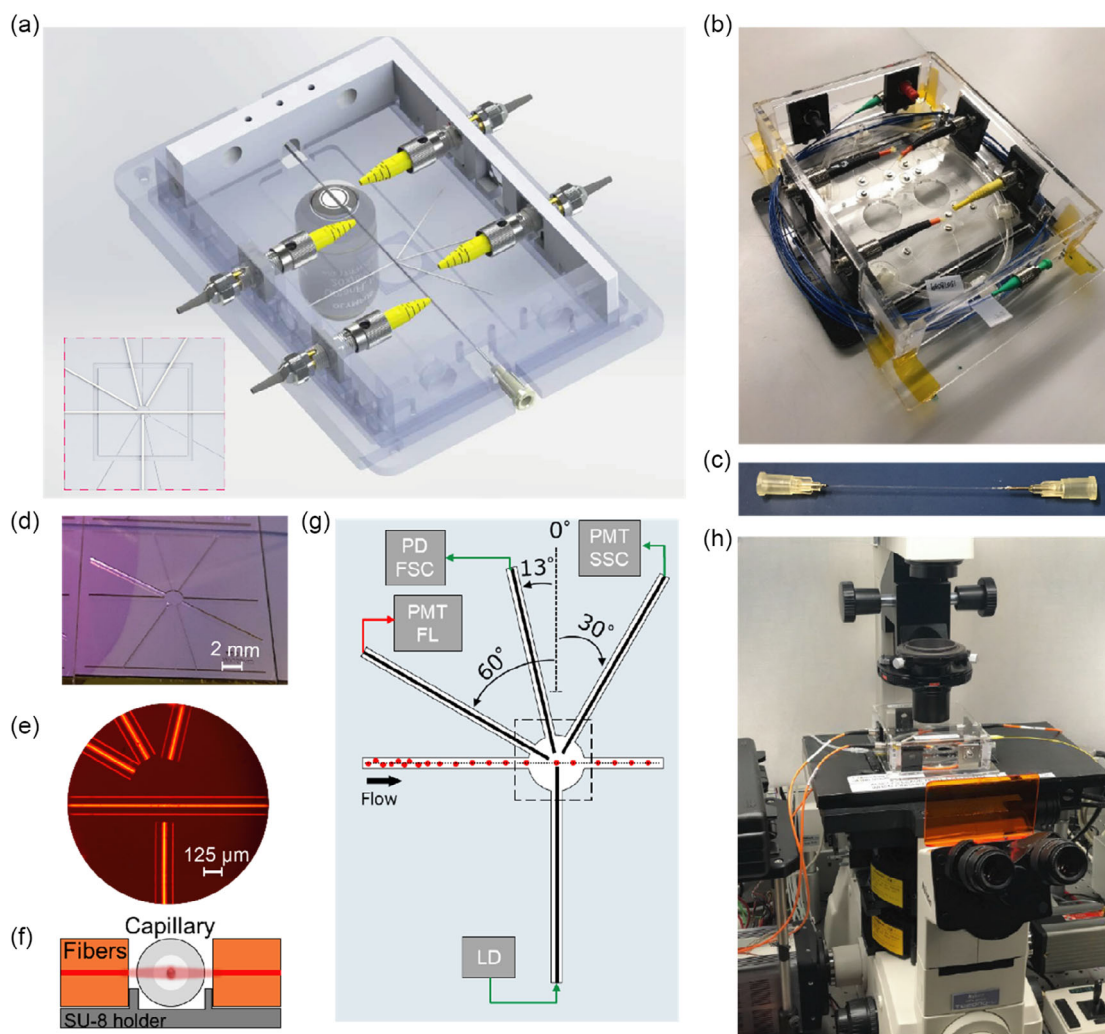


**Figure 1.** a) Schematic illustration of the viscoelastic capillary flow cytometry platform; small thumbnail is a close-lookup image to show the placements of microcapillary and optical fibers. b) Photo of the assembled flow cytometry platform: PMMA holder, optical fibers, fiber connectors, screw rings, and screws (microcapillary is not placed). Black-colored crown PMMA part is an adapter for the inverted microscope stage. c) Photo of the microcapillary channel. d) Photo of the microfabricated SU-8 holder. Optical fiber ends and microcapillary placed on the grooves on SU-8 jig and precisely aligned to each other. Then SU-8 holder is placed to the slot reserved on the PMMA holder shown in (a). e) Microscope image of the laser interaction region showing the end tips of optical fibers and microcapillary. f) The cross-sectional schematic view of the optical fibers and microcapillary alignment on the SU-8 jig. g) Schematic illustration of assembled components (not to scale). h) Photo of the flow cytometry platform while an experiment runs on an inverted microscope. External optical fibers are connected to the mating sleeves on the PMMA holder. The pressure pump is connected to the inlet of the microcapillary.

**Table 1.** The range of particles, particle sizes, and capillary inner diameters used in this study.

| Capillary code | Inner diameter<br>[μm] | Particle/cell   | Size<br>range [μm] | Blockage<br>ratio      |
|----------------|------------------------|-----------------|--------------------|------------------------|
| TSP030150      | 30                     | PS              | 2.0, 4.0, 6.0      | $0.07 < \beta < 0.2$   |
| TSP030150      | 30                     | PS              | 2.5, 4.0, 7.0      | $0.083 < \beta < 0.23$ |
| TSP030150      | 30                     | PLGA            | 0.5–6              | $0.016 < \beta < 0.2$  |
| TSP030150      | 30                     | Chromosomes     | 0.8–1.8            | $0.026 < \beta < 0.06$ |
| TSP050150      | 50                     | Erythrocytes    | 6–10               | $0.12 < \beta < 0.2$   |
| TSP075150      | 75                     | THP-1 Monocytes | 10–20              | $0.16 < \beta < 0.26$  |

Mikrolab Århus A/S) were used for the experiments with different size ranges of particles, as given in Table 1. A 30 μm ID capillary was used for PS beads (size range 2 to 7 μm), PLGA particles (diameter app. 1 to 3 μm), and mitotic chromosomes (size range 0.8 to 1.8 μm); a 50 μm ID capillary was used for red blood cells (size range 6 to 10 μm); and a 75 μm ID capillary was used for THP-1 leukemic cells (size range 10 to 20 μm) experiments. Twelve centimeters long capillaries were cleaved from both ends, and their coatings were stripped in an oven (Kruss, 650 °C, 2 h). Later, both capillary ends were UV glued to Gauge 27 syringe tips (Drifton) to form the inlet and outlet connections (Figure 1c). At last, the capillary was placed on its dedicated groove on the SU-8 jig and fixed to the laser-cut PMMA holder.

The SU-8 jig (Figure 1d) was fabricated in a cleanroom (DTU, Nanolab) to precisely align the central axes of the fibers and the capillary. A thin film (35 nm) of poly-Si was deposited on a 4 inch borosilicate glass wafer (Tempress LPCVD polysilicon furnace, SiH<sub>4</sub> flow 80 sccm, 620 °C, 200 mTorr) to enhance the adhesion of the SU-8 resist to the substrate. Then a 90 μm thick SU-82 035 photoresist film (Microchem) was spin-coated (SUSS Microtech Spinner) at 500 rpm 55 s (spread cycle) and 3500 rpm, 40 s (spin cycle). The resist layer was then soft-baked (2 min at 65 °C, 7 min at 95 °C, 1 min at 65 °C), UV exposed (220 mJ cm<sup>-2</sup>, Maskless Aligner MLA100, Heidelberg Instruments GmbH), post baked (3 min at 65 °C, 7 min at 95 °C, 1 min at 65 °C), developed (5 min), and hard-baked (95 °C, 15 h). Later, the glass wafer was diced (Dicing Saw) to 18 × 18 mm<sup>2</sup> squares and fixed on the laser-cut PMMA holder. Finally, the stripped fiber ends (strip length 15 mm) and the capillary were fixed on the SU-8 jig grooves using adhesive tape (Figure 1e). A schematic cross section of the alignment is given in Figure 1f.

The input laser, used for scattering and fluorescence excitation, was coupled to a single-mode optical fiber (core diameter 4.3 μm, cladding diameter 125 μm, P1-460B-FC-1, Thorlabs). The input laser fiber was placed perpendicular to the capillary. Three multimode fibers were placed on the opposite side of the capillary and used for the detection of scattered light (FSC fiber: core diameter 50 μm, cladding diameter 125 μm, M42L01, SSC and FL fibers: core diameter 110 μm, cladding diameter 125 μm, M43L01). The FSC fiber was placed at an angle of 13° to prevent the coupling of the direct laser input from the excitation laser light (Figure 1g).<sup>[10,29]</sup> The SSC and FL detection

fibers were placed at angles of 30° and 60° relative to the input laser fiber.

A pigtailed laser diode (15 mW, 520 nm, LP520-SF15, Thorlabs) was used as the input laser. A Si photodetector (DET025AFC/M, Thorlabs) was fiber connected for the signal detection in the FSC channel, and two PMT detectors were fiber connected to the SSC (H7827, Hamamatsu) and FL (H98280, Hamamatsu) channels. A dichroic mirror (MD588, Thorlabs), Notch Filter (NF533-17, Thorlabs), and 630/69 emission filter (MF630-69, Thorlabs) set was placed in a filter box and connected in front of the PMT detector for fluorescence detection in the FL channel. The all-connected platform was placed on an inverted microscope (Nikon TE2000-U) (Figure 1h). A high-speed camera (AOS S-MOTION) was used to record videos of particle trajectories at 1000 fps for low flow rates, 30 μL h<sup>-1</sup> and 5000 fps for higher flow rates up to 480 μL h<sup>-1</sup> flow rates. The recorded videos were split into single frames and image stacked to show the particle trajectories at the capillary axis.

#### 2.4. Design and Working Principle of the Viscoelastic Microfluidic Flow Cytometers Platform

Figure 1g schematically illustrates the working principle of the flow cytometry platform. Suspended particles (red spheres) in viscoelastic solutions migrate to their equilibrium positions at the capillary axis under a pressure-driven flow. The viscoelastic polymer molecules added to the buffer (or cell medium) induce a normal stress gradient – normal to the velocity field.<sup>[63]</sup> This results in an elastic lift force on particles in the flow that directs particles from the high shear rate (capillary wall) to the low shear rate regions (capillary axis) inside the capillary. Focused particles at the capillary axis interact with the incident laser light at the laser interaction region (black dashed square) and scatter laser light in the forward and side directions. Scattered and fluorescently emitted light signals are collected with multimode fibers and detected with photodetectors. The detected signals are collected and analyzed in real-time using a LabVIEW DAQ environment.

Central alignment of polydisperse suspensions of particles, of diameters,  $d \in [d_{\min}; d_{\max}]$  is required for flow cytometry. In viscoelastic flow focusing, there is a lower limit,  $d_{\min}$  to the range of particle diameters that can be focused in a given capillary of inner diameter,  $D$ .<sup>[63]</sup> The viscoelastic flow focusing efficiency scales with the so-called blockage ratio  $\beta = d/D$ . With a given capillary inner diameter  $D$ , rheological properties of the viscoelastic solution, and flow velocity, smaller particles (smaller values of  $\beta$ ) require a longer travel distance in the capillary to reach a stable particle alignment at the capillary axis.

As a rule of thumb, the relation  $\beta > 0.1$  (or  $d_{\min} > 0.1D$ ) will ensure stable particle alignment at the capillary axis at a few cm travel distance.<sup>[63]</sup> On the other hand, the condition  $D > d_{\max}$  should be respected to avoid clogging of the capillary. In addition, off-center alignment, due to modifications of the elastic force around the particle, has been reported in several studies for  $\beta > 0.25$ .<sup>[53,62–65]</sup> Consequently, to reach a stable particle alignment, the condition  $\beta < 0.25$  should be satisfied for the experimented size range of particles.

The elastic lift force depends on the viscoelastic fluids' rheological properties, flow conditions, and channel geometry. We prepared 1000 and 5000 ppm HA viscoelastic solutions in MQ Water, PBS, and FB solutions to promote biocompatibility for cell experiments.<sup>[50]</sup> It is reported that addition of physiological buffer to HA alters the shear-thinning properties and elasticity of the solution due to the shrinkage of the polyelectrolytes.<sup>[59,78]</sup> Our shear viscosity measurements also show that the shear-thinning profile of 1000 ppm HA in MQ water is smoothened, and nearly constant shear viscosity was obtained for HA viscoelastic solutions in PBS or FB medium (Supplementary file S1, Supporting Information). Particle focusing on shear-thinning solutions shows off-center alignment and applies in particle separation studies.<sup>[78]</sup> However, we aim to reach stable viscoelastic focusing along the capillary axis for a wide range of flow rates. Thus, a weak shear thinning, or near constant shear viscosity profile is beneficial for our flow cytometry experiments.

## 2.5. Real-Time General User Interface Platform (Elasto-μFlow) and Signal Analysis

The voltage output of the photodetectors detecting forward scattered, side scattered, and fluorescence signals were connected to a multifunctional DAQ card (USB-6351, National Instruments) with a multichannel maximum sample rate of  $1.25 \text{ MS s}^{-1}$ . The analog inputs were connected in differential mode and shared the common ground to reduce environmental noise. To avoid crosstalk due to floating charge injection between the three detection units, neighboring units were separated by one grounded input terminal. In total, three detection channels and three grounded channels were used with a maximum sampling rate of  $100 \text{ kS channel}^{-1}$ .

The block diagram and detailed description of the real-time detection algorithm are given in the supplementary file S7, S8, Supporting Information. The scattering signals are read into LabVIEW (National Instruments) using a NI-DAQmx driver controlling the timing of the data acquisition. These data are sampled continuously with the user-defined sample rate and number of samples. These two parameters determine a buffer, i.e., a temporary storage where the data are stored to be fed into the acquisition. The sample rate should be determined from the highest frequency of scattering events to have a sufficient resolution of the peaks in the scatter signals. The number of samples corresponds to the buffer size and should be chosen large enough to avoid overflowing the buffer while processing the data. A sampling rate of  $100 \text{ kS s}^{-1}$  (maximum sampling rate per channel) was used in this study to stay within the limits of the DAQ card and correspondingly 100 k samples were read at a time making the buffer size sufficiently large for real-time processing. A real-time LabVIEW GUI platform, Elasto-μFlow, was developed to handle the data acquisition and processing of the signals as well as controlling the pressure pump (Fluigent MFSC) in a Producer/Consumer Architecture. The Producer/Consumer pattern allows for fast and efficient data acquisition with minimal data loss (Producer) in parallel with more demanding real-time analysis of the scatter signals (Consumer) without slowing down the application. Elasto-μFlow collects the real-time signal and post-processes it to analyze characteristics of the scattering

events such as peak amplitude, area, width, and time stamps. Voltage signal outputs, scatter plots, and histograms in real time with/without gating is displayed as the output in common with commercial flow cytometry GUIs, etc. DIVA.

The throughput of the demonstrated MFC platform is limited by the sampling rate of the applied DAQ card. Using  $2 \text{ MSa s}^{-1}$  sampling rate oscilloscope (Agilent, MSO7104A) with post signal processing a throughput of  $3500 \text{ particles s}^{-1}$  using  $2 \text{ MSa s}^{-1}$  was achieved, see processing in Figure S13, Supporting Information.

## 2.6. Ethics

The use of anonymized donor material is covered by the general ethical approval for use of donor material for normal controls and in compliance with Transfusion Medicine Standards (TMS) of Danish Society of Clinical Immunology (DSKI). A written consent to participate as anonymized normal control was obtained from each of the participating donors as part of standard practice at the blood bank at Rigshospitalet, Copenhagen University Hospital, Copenhagen, Denmark. Donors participated in compliance with the Helsinki Declaration. All data were anonymously analyzed.

## 3. Results and Discussion

As discussed in the Methods section, efficient viscoelastic flow focusing relies on the balance between particle size, capillary diameter, rheological parameters, and flow rate, parameterized via the blockage ratio ( $\beta$ ). Calibration experiments using a  $30 \text{ μm}$  ID capillary and PS beads suspended in 1000 ppm FB-HA viscoelastic medium yielded stable and single-train particle focusing for bead diameters from  $6 \text{ μm}$  down to  $2 \text{ μm}$  at a distance of  $7 \text{ cm}$  from the inlet (Supplementary File S9, Supporting Information). Hence, the optical interaction region was placed at this distance. Similar experiments were performed with  $50$  and  $75 \text{ μm}$  ID capillaries to cover the full particle size range from  $2$  to  $20 \text{ μm}$  (see Figure S10 and S11, Supporting Information). For a given particle diameter, a suitable capillary ID can be chosen as shown in Table 1 and easily inserted in the platform as illustrated in the movie (Supplementary video S14, Supporting Information).

### 3.1. Flow Cytometry Measurements

To demonstrate the versatility of the viscoelastic flow cytometer with effortless capillary exchange, we performed flow cytometry experiments on a range of different types of synthetic and biological particles: PS calibration beads, PLGA particles, erythrocytes, THP-1 leukemic monocytes, and human metaphase chromosomes. For all types of samples, the performance of the viscoelastic flow cytometer was validated by benchmarking against a commercial flow cytometer, the BD Fortessa.

#### 3.1.1. Size Detection and Particle Counting of Polystyrene and PLGA Particles

Figure 2 shows the experimental results for calibration and performance analysis of the viscoelastic flow cytometry.

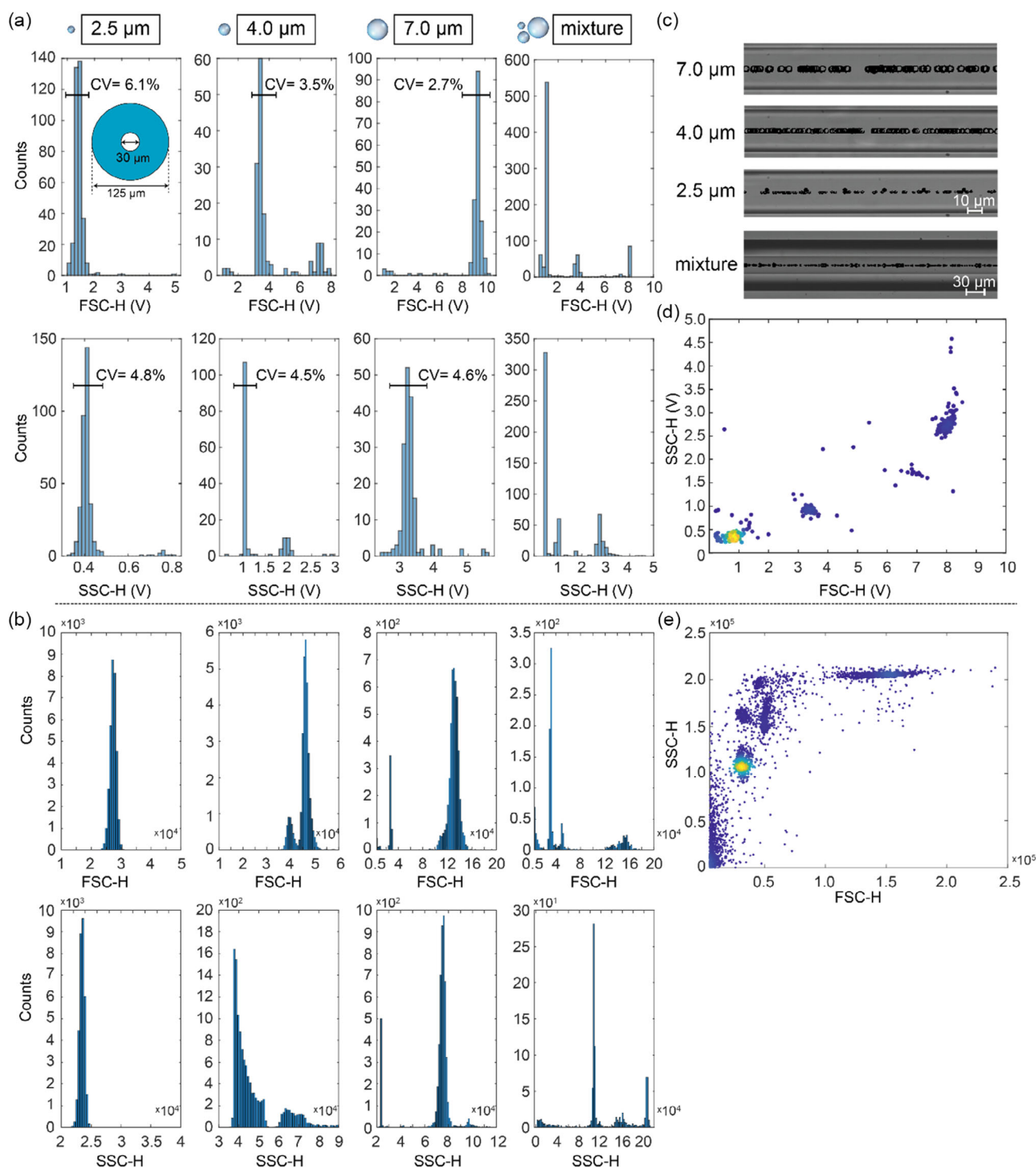


**Figure 2.** The comparison of the MFC and commercial BD Fortessa FC results for different size PS beads. 1<sup>st</sup>, 2<sup>nd</sup>, 3<sup>rd</sup>, and 4<sup>th</sup> columns in (a) and (d) show the histogram plots of counted events for 2.5, 4, 7  $\mu\text{m}$ , and polydisperse mixture suspension, respectively. MFC results show a) histogram plots for forward scatter (FSC) and side scatter (SSC) events, b) top-view image stacked photos of high-speed camera recordings for the best viscoelastic focusing condition ( $\Delta P = 1000$  mbar,  $Q = 25$   $\mu\text{L h}^{-1}$ ), and c) scatter plots of FSC-H to SSC-H events for the polydisperse mixture suspension. BD Fortessa FC results show d) histogram plots for forward scatter (FSC), and side scatter (SSC) events, and e) scatter plots of FSC-H to SSC-H events.

Measurements were performed using a 30  $\mu\text{m}$  ID capillary. Flow focusing and FSC/SSC signal detection performance were evaluated using 2.5, 4, and 7  $\mu\text{m}$ -diameter monodisperse and

all-mixed polydisperse PS particle suspensions. FSC and SSC histogram plots for experiment sets are given in Figure 2a,b (columns 1 to 4 represent each set of experiments). Figure 2c

shows the image-stacked photos of fully developed viscoelastic focusing at the capillary axis for each experiment set at  $25 \mu\text{L h}^{-1}$  flow rate ( $Re = 0.06$ ,  $Wi = 19$ ,  $El = 326$ ). The MFC experiments in Figure 2a were conducted at the best focusing condition, as shown in Figure 2c.

We used the detected peak height values (FSC-H and SSC-H) to generate histogram plots for cytometry measurements in Figure 2a, b. The total number of  $\approx 10^3$  events counted in 10 s for MFC and  $10^4$  events counted in 60 s for BD Fortessa measurements. The coefficient of variation values (defined as the standard deviation divided by the mean of the signal intensity) were calculated to be 6.1%, 3.5%, and 2.1% for FSC-H and 4.8%, 4.5%, and 4.6% for SSC-H for 2.5, 4, and  $7 \mu\text{m}$ -diameter experiments, respectively. Gating above 90% was applied on CV% calculations to exclude statistical outliers such as doublets, triplets, and clumps, as shown with the whisker bar on the histogram plots. Higher CV% values are expected for  $\beta < 0.1$  due to low induced elastic lift force-related positional fluctuations at the capillary axis. Nevertheless, 6.1% FSC-H and 4.8% SSC-H CV% values are in the range of state-of-the-art flow cytometry results provided by the BD Fortessa.

It is expected to measure higher FSC-H voltage levels by increasing the bead size and finally reaching saturation at the

photodetector. Therefore, the measurement resolution of the MFC device should be characterized by the expected range of particles. We performed resolution characterization by 2.5, 4, and  $7 \mu\text{m}$  diameter mixture particle suspension measurements. Each size PS particle in the mixture suspension is populated at their distinct FSC-H and SSC-H voltage levels without saturating the detectors. Different size clusters are clearly observed in FSC-H vs. SSC-H scatter plots given in Figure 2d. BD Fortessa experiments with the same particle concentrations for each set showed a similarly distributed histogram and FSC-H vs SSC-H scatter plots in Figure 2b,e. It should be noted that FSC-H and SSC-H values differ for both MFC and BD Fortessa measurements since detector threshold and gain levels are user dependent and specific to each experiment, thus set differently for both measurement devices.

Figure 3 shows the results for the second set of flow cytometry experiments using elastic PLGA particles for MFC experiments. PLGA particles are fabricated by the emulsion-solvent evaporation technique, and their size was determined using light microscopy and ImageJ software. Herein, an average diameter of  $1.9 \pm 0.9 \mu\text{m}$  with a 0.2 PDI was obtained. Six independent PLGA particle batches were assessed, showing the total range

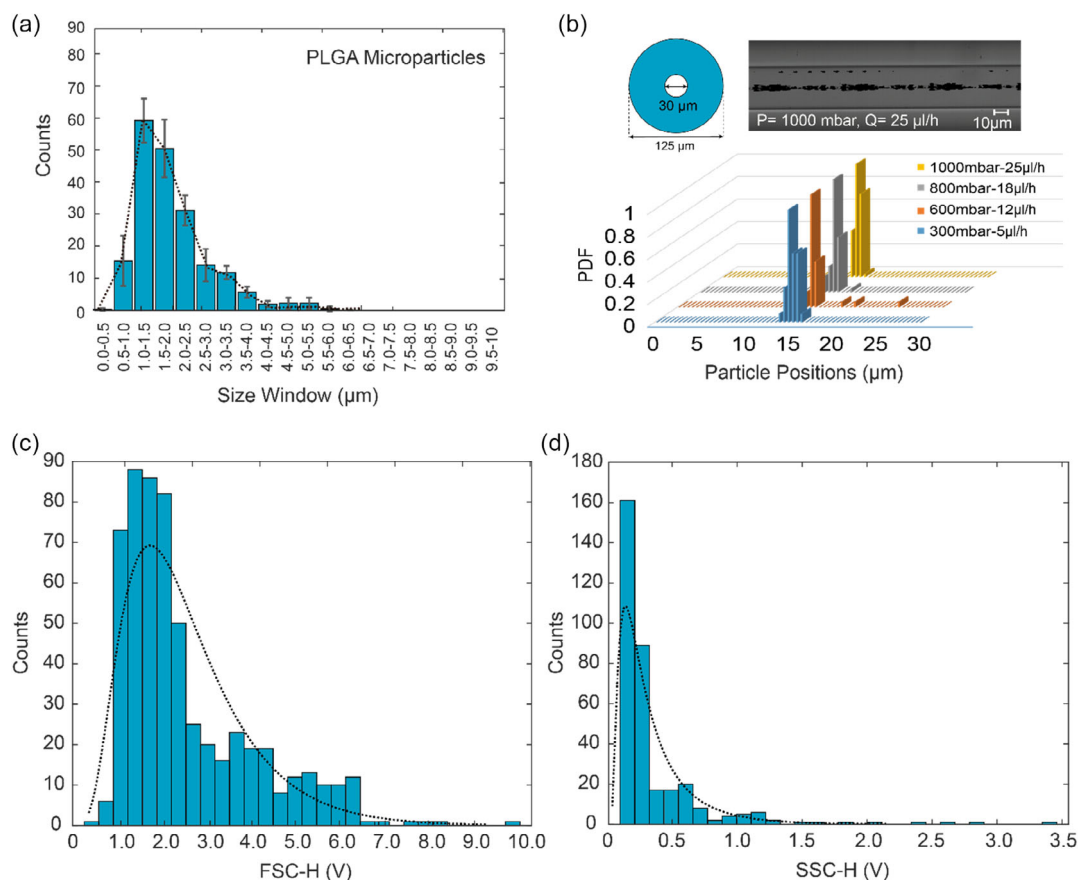


**Figure 3.** MFC measurement results for poly lactic-co-glycolic acid (PLGA) particles. a) The size measurement of synthesized PLGA particles shows the polydispersity of PLGA particles. b) Top-view image stacked photo of high-speed camera recording for the best viscoelastic focusing condition ( $\Delta P = 1000 \text{ mbar}$ ,  $Q = 25 \mu\text{L h}^{-1}$ ). PDF of particle distributions with PLGA particles across the cylindrical capillary microchannel cross section at a 7 cm distance from the inlet for different flow rates. MFC results showing c) histogram plots for FSC events and d) histogram plots for SSC events on PLGA particle suspension ( $\Delta P = 1000 \text{ mbar}$ ,  $Q = 25 \mu\text{L h}^{-1}$ ). Capillary inner diameter is 30  $\mu\text{m}$ .

of diameters obtained varied between 0.5 and 6  $\mu\text{m}$  (only one batch is given in Figure 3a). Within each batch, at least 200 particles in five areas were measured. PLGA particles are elastic and polydisperse compared to commercially available monodisperse PS particles, and their size range should be assessed always after they are synthesized with manual size measurements under microscope. Thus, it is beneficial to evaluate the sizing performance of our flow cytometry platform with PLGA particles.

Figure 3c,d shows the MFC experiment results with histogram plots generated from FSC-H and SSC-H channels. A total number of app. 100 events were detected in 1 s. The FSC-H peak amplitude distribution in Figure 3c agrees with the size distribution extracted from microscope images, as shown in Figure 3a. The consistency between the measured size distribution in Figure 3a and the voltage distribution in Figure 3b confirms that the MFC device can be used for size calibration of synthetically fabricated, polydisperse particles.

### 3.1.2. Viscoelastic Flow Cytometry on Human Cells and Chromosomes

MFC experiments were performed on biological samples such as human blood, THP-1 cells, and chromosomes.

Whole blood components have cells of varying sizes up to  $d_{\text{max}} = 15 \mu\text{m}$ . We investigated the viscoelastic focusing performance of 15  $\mu\text{m}$  diameter size polystyrene beads ( $\beta = 0.5$ ), which resulted in off-axis alignment at the 30  $\mu\text{m}$  ID fused silica capillary (Supplementary file S10, Supporting Information). Therefore, the 30  $\mu\text{m}$  ID capillary was swapped with a 50  $\mu\text{m}$  ID fused silica capillary to be used as the flow cell for blood cells. For the studied erythrocytes with sizes ranging from 6 to 10  $\mu\text{m}$ , the blocking ratio satisfied  $0.1 < \beta < 0.2$ .

To investigate the viscoelastic focusing performance, RBCs were isolated from human whole blood and suspended in 1000 ppm FB-HA viscoelastic solution (protocol explained in material and methods section). The cell suspension was pumped through the capillary inlet, and a video was recorded with a high-speed camera to analyze the performance of viscoelastic focusing at flow rates ranging from 8 ( $Re = 0.01$ ,  $Wi = 1.32$ ,  $El = 117$ ) up to  $120 \mu\text{L h}^{-1}$  ( $Re = 0.17$ ,  $Wi = 20$ ,  $El = 117$ ).

Figure 4a shows the image-stacked photos of a suspension of erythrocytes centrally aligned on the capillary axis. Figure 4b shows the calculated PDF values to show the radial particle distribution at the capillary cross section. Stable viscoelastic focusing was reached for all applied flow rates.

Due to their high deformability, RBCs are influenced by elastic as well as deformation lift forces in the viscoelastic solution.

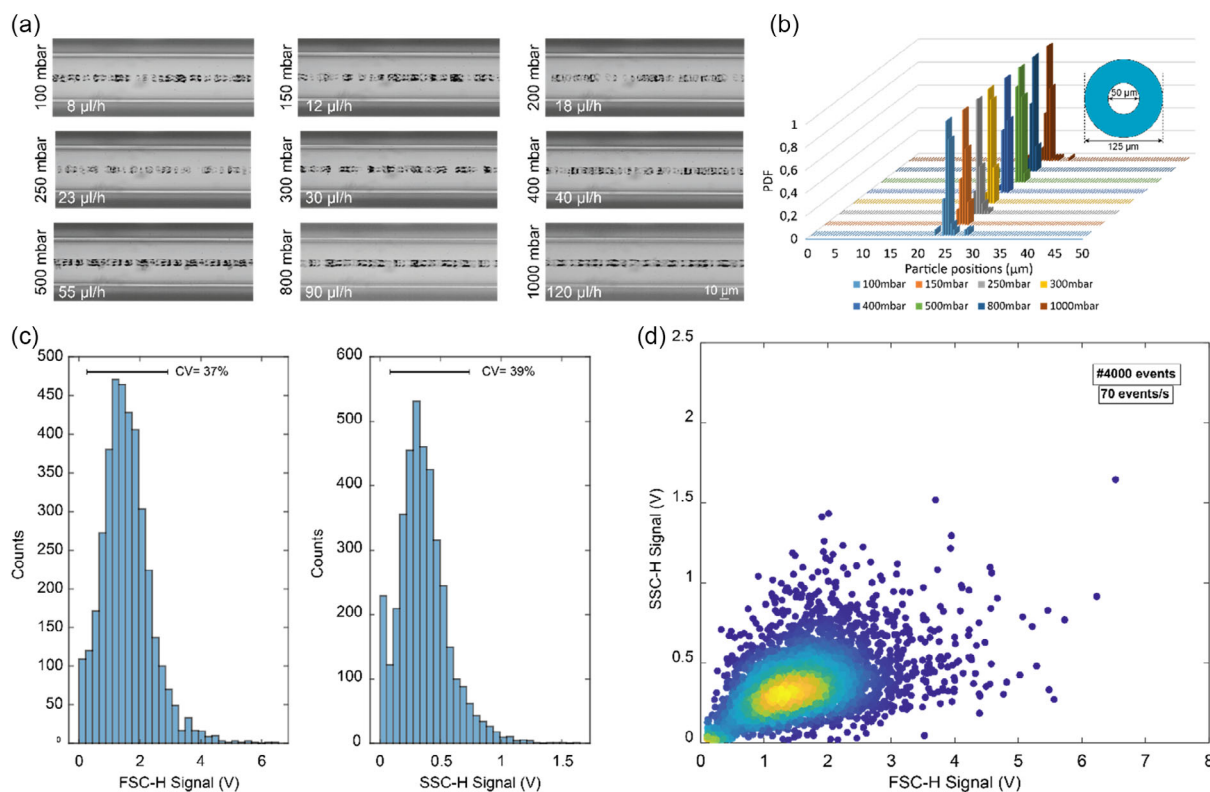


**Figure 4.** MFC measurement results for human blood experiments (red blood cells). a) Top-view image stacked photos of high-speed camera recordings showing stable viscoelastic focusing for the entire working range of pressure pump starting from 100 mbar up to 1000 mbar. The capillary inner diameter is selected as 50  $\mu\text{m}$  to reach stable viscoelastic focusing for red blood cells in a wide range of flow rates starting from 8  $\mu\text{L h}^{-1}$  up to 120  $\mu\text{L h}^{-1}$ . b) PDF of particle distributions with red blood cells across the cylindrical capillary microchannel cross section at a 7 cm distance from the inlet with different flow rates. MFC results show c) histogram plots for FSC-H and SSC-H events and d) scatter plots of FSC-H to SSC-H events. Throughput is 70 events  $\text{s}^{-1}$  at 1000 mbar and 120  $\mu\text{L h}^{-1}$  flow rate. Cell density is  $\approx 10^6$  RBCs  $\text{mL}^{-1}$  for all the experiments.

Therefore, it was possible to align RBCs for a wide range of flow rates (in the spectrum of this study) at the capillary axis. It is also observed that RBCs formed a parachute shape at flow rates above  $30 \mu\text{L h}^{-1}$ . Such shape formation reduces the orientation-related variations in cytometry measurements,<sup>[59]</sup> relaxing the need to use reagents to transform RBCs into a spherical shape.<sup>[29]</sup>

Figure 4c and 5d shows the MFC experiment results with histogram distribution of events from FSC-H and SSC-H detection and FSC-H vs. SSC-H scatter plots. A total number of 4000 events were detected in 1 min corresponding to a throughput of  $70 \text{ events s}^{-1}$  at a flow rate of  $120 \mu\text{L h}^{-1}$  for a 500 times diluted cell suspension. The detected events are concentrated at app. 1.5 V FSC-H and 0.25 V for SSC-H channels. The distribution of fleeing particle events (omitted in histogram plots) can be seen in the bottom-left corner of the scatter plot in Figure 4d. Due to their small size and off-axis alignment, they have small scattering signals for both FSC-H ( $<0.3 \text{ V}$ ) and SSC-H ( $<0.1 \text{ V}$ ) channels.

These results demonstrate the performance of the MFC device for highly efficient and stable RBC focusing with low axial alignment variations. High-performance flow cytometry with  $100 \text{ events s}^{-1}$  throughput is achieved.

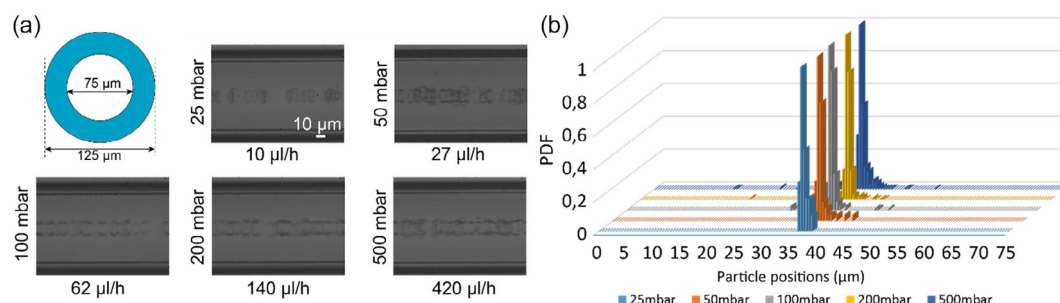
We continued MFC experiments using a human leukemic monocyte-like cell line. Initial experiments were demonstrated using 30 and  $50 \mu\text{m}$  ID capillaries to support efficient viscoelastic focusing while satisfying channel blockage ratio at  $0.1 < \beta < 0.2$ . The monocytes used in these experiments had a diameter range of  $15 \pm 5 \mu\text{m}$ .

A  $75 \mu\text{m}$  ID capillary was used to avoid off-center particle alignment (due to large blockage ratio) and clogging in case of cell doublets or triplets present in the flow. Efficient particle focusing was ensured by satisfying  $0.15 < \beta < 0.25$  for the used capillary and given cell diameters.

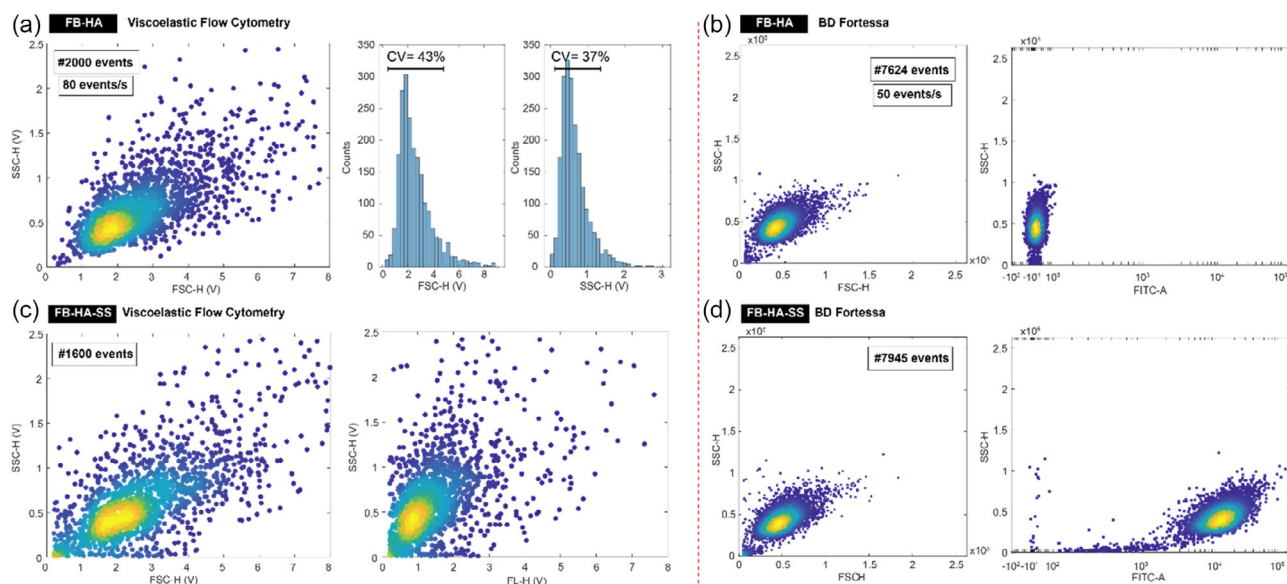
Figure 5a shows the image-stacked photos of centrally aligned cells along the capillary axis. Figure 5b shows the calculated PDF values for radial particle distribution at the capillary cross section. Viscoelastic focusing was always stable at the capillary axis for a wide range of flow rates starting from  $10 \mu\text{L h}^{-1}$  ( $Re = 0.009$ ,  $Wi = 0.49$ ,  $El = 52$ ), reaching up to  $420 \mu\text{L h}^{-1}$  ( $Re = 0.4$ ,  $Wi = 20$ ,  $El = 52$ ). The PDF values showed similar profiles for each flow rate. In common with the RBCs, deformation lift forces contribute to the elastic lift force to reach a stable viscoelastic cell focusing.

Figure 6 shows the flow cytometry experiments performed with THP-1 monocytes. The cells were stained with a viability stain (SS), fixed and suspended to FB-HA viscoelastic medium, to detect the fluorescence signal (FL) together with the FSC and SSC signals. MFC experiments were performed at  $420 \mu\text{L h}^{-1}$  (mid-flow rate at 500 mbar), yielding a throughput of  $80 \text{ events s}^{-1}$  with a total number of 2000 cells in 25 s. BD Fortessa experiments were performed at mid-flow rate settings (app.  $60 \mu\text{L min}^{-1}$ ), yielding a throughput of  $50 \text{ events s}^{-1}$  with a total of app. 7600 cells in 150 s. For the sake of equal comparison, a pump pressure of 500 mbar was used (mid-flow rate: considering max output is 1000 mbar) during MFC measurements using the same cell population. We present flow cytometry measurements from both unstained (Figure 7a,b) and stained (Figure 7c,d) THP-1 cells. Figure 6a shows the scatter plot of FSC-H versus SSC-H and histogram plots of FSC-H and SSC-H detection for MFC experiments. Figure 6b shows the scatter plots of FSC-H versus SSC-H and FITC-A versus SSC-H for BD Fortessa experiments. BD experiments, shown in Figure 6b, also provide autofluorescence measurements; however, this measurement is not possible with the low-cost PD and PMT detectors used in the MFC device. We also investigated the 8-peak fluorescent intensity measurements using 8-peak rainbow beads in Figure S12, Supporting Information. However, due to low dynamic range of the low-cost PMTs, we could only resolve 5-peaks of 8-peak fluorescent intensities. Figure 6c shows the scatter plots of FSC-H versus SSC-H and FL-H versus SSC-H for MFC experiments. Figure 6d shows the scatter plots of FSC-H versus SSC-H and FITC-A versus SSC-H for BD Fortessa experiments. According to the side-by-side comparison of all the results in Figure 6a–d, all the experiments showed a similar distribution of well-focused cells with a similar throughput range as indicated in the figure. It is possible to detect fluorescently stained cells with the MFC device with a similar accuracy to BD Fortessa.

Flow cytometry systems have played a pivotal role in deciphering the sequence of the human genome by analyzing and isolating human chromosome populations.<sup>[79]</sup> Human metaphase chromosomes are condensed structures of DNA and protein and have dimensions of  $4.38 \pm 1.97 \text{ cm}$ , 250 Mbp linear length, and  $\approx 12 \text{ Å}$  radius as a single DNA molecule. Condensed metaphase chromosomes are stabilized in a rod-like canonical shape with lengths varying between 2–8  $\mu\text{m}$  and widths between



**Figure 5.** Viscoelastic particle focusing experiment for THP-1 human leukemic monocytes. a) Top-view image stacked photos of high-speed camera recordings showing stable viscoelastic focusing on a wide range of flow rates starting from  $10 \mu\text{L h}^{-1}$  up to  $420 \mu\text{L h}^{-1}$ . The capillary inner diameter is selected as  $75 \mu\text{m}$  to reach stable viscoelastic focusing for THP-1 cells b) PDF of particle distributions with THP-1 cells across the cylindrical capillary microchannel cross section at a 7 cm distance from the inlet for different flow rates.



**Figure 6.** The comparison of MFC and commercial BD Fortessa results for THP-1 human leukemic monocytes. Viscoelastic MFC results of a) scatter plot of FSC-H versus SSC-H events and histogram plots for FSC-H and SSC-H events and BD Fortessa results of b) scatter plots of FSC-H versus SSC-H and FITC-A versus SSC-H events, for unstained THP-1 cells. Viscoelastic MFC results of c) scatter plots of FSC-H versus SSC-H and FL-H versus SSC-H events and BD Fortessa results of d) scatter plots of FSC-H versus SSC-H and FITC-A versus SSC-H events, for stained (SS) THP-1 cells. Throughput is 80 events  $s^{-1}$  at 500 mbar and  $420 \mu L h^{-1}$  flow rate for viscoelastic MFC and 50 events  $s^{-1}$  at MID range flow rate settings ( $17.5$  to  $70 \mu L min^{-1}$ ) for BD Fortessa. Cell density is  $\approx 10^6$  cells  $mL^{-1}$  for all the experiments. (Capillary inner diameter is  $75 \mu m$ ).

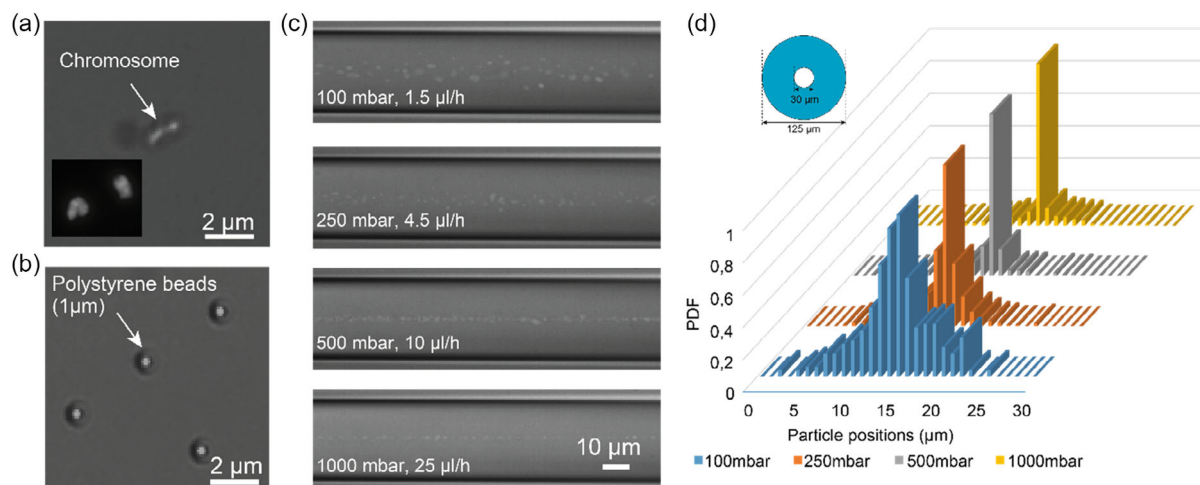


**Figure 7.** Viscoelastic particle focusing experiment for human metaphase human chromosomes. a) Bright-field microscope images of a single chromosome at  $100\times$  magnification. (Small capture is taken with a fluorescent microscope from GFP-stained chromosomes at 3-second exposure of  $470$  nm light excitation source.) b) Bright-field microscope images of  $1 \mu m$  size PS beads. c) Top-view image stacked photos of high-speed camera recordings showing stable viscoelastic focusing on a wide range of flow rates starting from  $1.5 \mu L h^{-1}$  up to  $25 \mu L h^{-1}$ . d) PDF of particle distributions with chromosomes across the cylindrical capillary microchannel cross section at the  $7$  cm distance from the inlet for different flow rates. The capillary inner diameter is selected as  $30 \mu m$ .

$0.25\text{--}0.5 \mu m$ .<sup>[80]</sup> Due to their small size and nonuniform shape, chromosomes would be a good case study to test viscoelastic flow focusing and perform flow cytometry experiments with our MFC device.

Figure 7 shows viscoelastic flow focusings of chromosomes at different flow rates in a  $30 \mu m$  ID capillary. The applied pressure was set to 100, 250, 500, and 1000 mbar (max), corresponding to flow rates of 1.5, 4.5, 10, and  $25 \mu L h^{-1}$ ,

respectively. The metaphase chromosomes used in the experiment are ultrapurified from other cell debris, as described in the Material and Methods section. Figure 7a,b shows bright-field microscopy images of chromosomes and their size estimation in comparison to  $1 \mu m$  diameter PS beads. The equivalent chromosome diameter varies between  $0.7$  and  $1.8 \mu m$  satisfying the channel blockage ratio of  $0.02 < \beta < 0.06$  in the  $30 \mu m$  ID capillary.

Figure 7c,d shows image stacked photos of top-view high-speed camera recordings along the capillary axis and PDF values at the capillary cross section. Radial chromosome alignment improved gradually with increasing flow rates. The flow rate at  $10 \mu\text{L h}^{-1}$  shows good viscoelastic flow focusing and best axial alignment, with the lowest radial variation observed at the highest flow rate,  $25 \mu\text{L h}^{-1}$ . The induced elastic force is weak due to the nonspherical canonical shape of chromosomes and their low blockage ratio ( $\beta < 0.1$ ) with the  $30 \mu\text{m}$  ID capillary channel. Thus, pumping the viscoelastic solution at the pressure pump's maximum output is required to reach a stable viscoelastic focusing.

**Figure 8** shows the flow cytometry experiments performed with metaphase chromosomes suspended in viscoelastic solution at a concentration of app.  $10^6$  chromosomes  $\text{mL}^{-1}$  cells. Chromosomes detected using m-Cherry fluorescence channel. To demonstrate the capability of the real-time GUI platform, we used peak area values (FSC-A, SSC-A, and FL-A) instead of peak height (FSC-H, SSC-H, and FL-H). Therefore, FSC, SSC, and FL channels are plotted using peak area values in Figure 8.

MFC experiments performed at  $25 \mu\text{L h}^{-1}$  yielded a throughput of  $40 \text{ events s}^{-1}$  with a total number of 1800 events detected in app. 1 min. The throughput for BD Fortessa experiments was

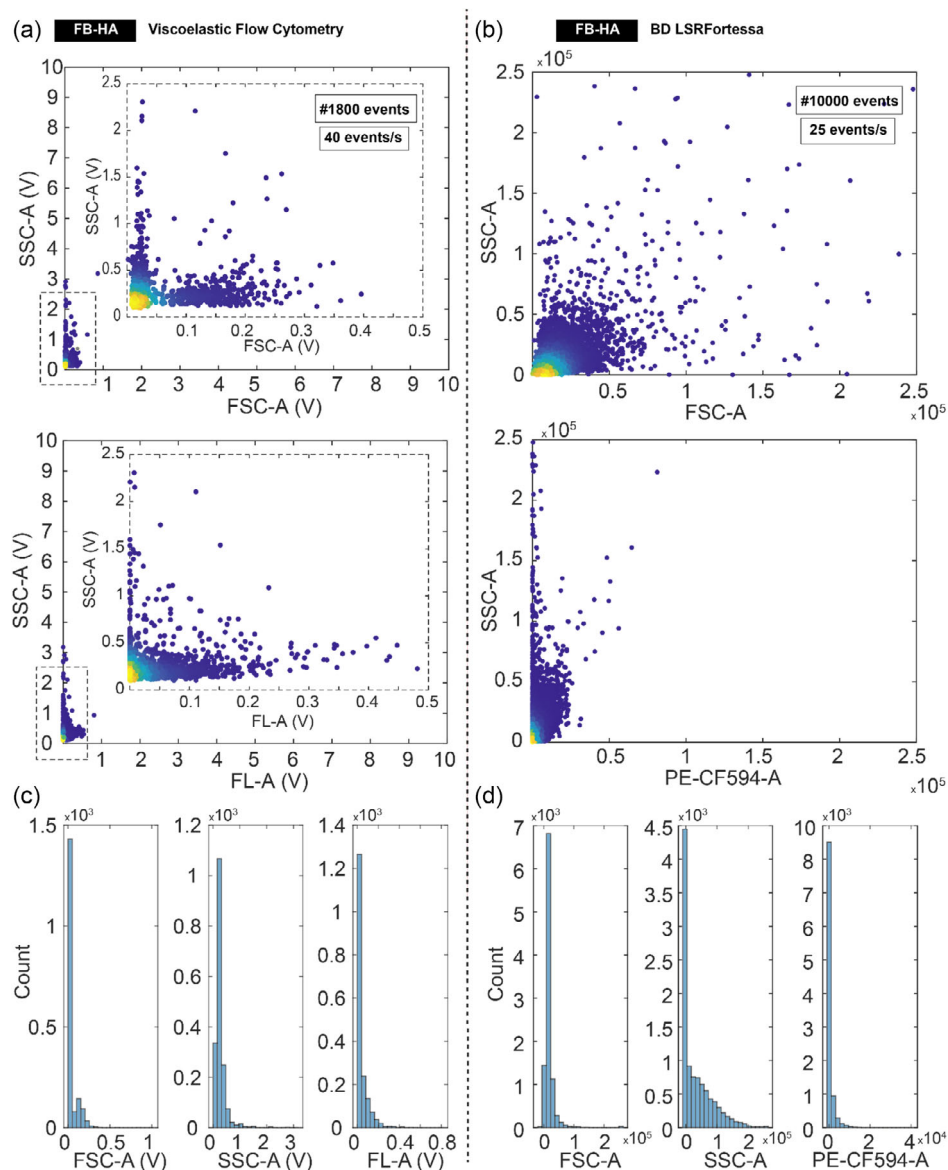


**Figure 8.** The comparison of MFC and commercial BD Fortessa FC results for metaphase human chromosomes. Viscoelastic MFC results of a) scatter plots of FSC-A to SSC-A and FL-A to SSC-A events for m-Cherry-stained chromosomes and b) histogram plots for FSC-A, SSC-A, and FL-A events. Throughput is  $50 \text{ events s}^{-1}$  at 1000 mbar and  $25 \mu\text{L h}^{-1}$  flow rate (capillary inner diameter is  $30 \mu\text{m}$ ). BD Fortessa FC results of c) scatter plots of FSC-A to SSC-A and PE-CF594-A to SSC-A events for m-Cherry-stained chromosomes and d) histogram plots for FSC-A, SSC-A, and PE-CF594-A events. Throughput is  $25 \text{ events s}^{-1}$  at MID range flow rate settings. Cell density is app.  $10^6$  chromosomes  $\text{mL}^{-1}$  for all the experiments.

25 events  $s^{-1}$  with 10 000 events in app. 7 min. Figure 8a,b shows the scatter plots and histogram plots of FSC-A, SSC-A, and FL-A detection for MFC and BD Fortessa experiments. Small insets in Figure 8a represent the black-colored dashed squares from MFC scatter plots to visualize the low amplitude signal closer to the origin.

Both experiments with the MFC and BD Fortessa showed similar trends in their histogram plots comparison in Figure 8c,d. The fluorescent signal was detected with the MFC device at a similar performance to BD Fortessa. Due to low elastic lift force and low-angle light scattering from nonuniform particle cross section, both forward and side-scattered signals have low amplitude compared to measurements done with spherical beads, large size erythrocytes, or THP-1 cells. Nevertheless, side-by-side comparison shows that viscoelastic flow focusing and flow cytometry experiments can be conducted with the proposed MFC device.

## 4. Conclusion

A compact microfluidic flow cytometry platform comprising viscoelastic flow focusing in fused silica capillaries and an integrated fiber optical interface has been demonstrated. FSC, SSC, and FL signals are collected. The developed system is mounted on an inverted microscope for easy integration with optical imaging and other optofluidic modalities, such as optical trapping and particle sorting. This allows robust, portable, and miniaturized solutions for implementing point-of-care flow cytometry tools.

The compact system is versatile. The device performance was benchmarked against a commercial flow cytometer, BD Fortessa, using PS calibration beads, PLGA particles, erythrocytes, THP-1 leukemic monocytes, and human metaphase chromosomes. Experiments with synthetic particles show low CV% values thanks to a highly stable viscoelastic focusing at the capillary axis. In addition, single-cell experiments with RBCs, THP-1 cells, and chromosomes benchmarked well with BD Fortessa measurements.

The system is modular and enables flow cytometry measurements using a single-inlet flow source and different inner diameter capillaries. This allows having the flexibility to select the optimal capillary size for a wide range of particle diameters ranging from 2 to 20  $\mu m$  (within the scope of this study). Supplementary video S14, Supporting Information demonstrates the versatility of our modular flow cytometry setup with capillary exchange method and walks the viewer through the building steps of the platform. The system can be further optimized for particle diameters smaller than 2  $\mu m$ , using smaller size ID capillary ( $D < 30 \mu m$ ) or a higher pump pressure ( $\Delta P > 1$  bar).

A real-time detection platform, Elasto- $\mu$ Flow, was used for data collection and analysis. A throughput of 100 particles  $s^{-1}$  was achieved with measurements at low Reynolds numbers. It is possible to support viscoelastic flow focusing even at much higher flow rates at  $Re = 2000$  using a mutual combination of elastic and inertial forces.<sup>[50]</sup> However, the maximum pressure drop along the capillary and low sampling rate in the real-time detection unit are the limiting factors. Hence, the throughput could be further increased by using a higher sampling rate real-time data acquisition unit and/or a higher pump pressure.

A twofold improvement could be achieved using a 10 Ms channel $^{-1}$  sampling rate DAQ unit with a throughput of app. 10 000 events  $s^{-1}$ . To support our claim about hardware optimization to reach high throughput, we demonstrated a throughput of 3500 particles  $s^{-1}$  using a 2 MSa  $s^{-1}$  sampling rate oscilloscope with post signal processing, see Figure S13, Supporting Information.

State-of-the-art flow cytometry assays include multicolor fluorescence detection. For example, two or more different DNA-binding dyes, labeling different base pairs, would enable automated chromosome karyotyping, replacing current time-consuming and labor-intensive methods. Also, precise flow focusing and particle alignment are essential due to low differences in DNA content between chromosomes. Hence, our platform is a promising tool for developing applications that combine automated chromosome isolation with a dedicated set of fluorescent filters and excitation lasers and utilize viscoelastic flow focusing to reach highly stable chromosome alignment at the capillary axis.

## Supporting Information

Supporting Information is available from the Wiley Online Library or from the author.

## Acknowledgements

This work was partly funded by NovoNordisk Foundation Interdisciplinary Synergy Programme, project ChromoCapture (Grant No.: NNF18OC0034948). C.F.N. and I.D.H. are supported by the Danish National Research Foundation (Grant No.: DNR115). M.N. and K.B.S. are supported by the Independent Research Fund Denmark (Grant No 0135-001428) and the Novo Nordisk Foundation (Grant No.: NNF20OC0061673). M.N. and K.B.S. acknowledge fruitful discussions with Martin Dufva. M.N. and M.S. acknowledge Bente Rotbøl for technical support on flow cytometry. M.S. acknowledges Per Thor Jonassen and Henning Engelbrecht Larsen for technical support during PMMA laser machining and low noise DAQ board connections. M.S. acknowledges productive discussions with Rodolphe Marie, Airidas Žukauskas, Mahmood Tawfiq, and Andreas Raimund Stilling-Andersen.

## Conflict of Interest

The authors declare no conflict of interest.

## Data Availability Statement

The data that support the findings of this study are available from the corresponding author upon reasonable request.

## Keywords

blood cells, capillary, chromosomes, flow cytometry, microfluidics, optofluidics, viscoelastic focusing

Received: October 7, 2022

Published online:

- [1] W. Dittrich, W. Göhde, Z. *Naturforsch. B* **1969**, 24, 360.
- [2] Y. Zhang, B. R. Watts, T. Guo, Z. Zhang, C. Xu, Q. Fang, *Micromachines* **2016**, 7, 70.
- [3] R. J. Yang, L. M. Fu, H. H. Hou, *Sens. Actuators, B Chem.* **2018**, 266, 26.
- [4] L. Zhang, X. Chen, Z. Zhang, W. Chen, H. Zhao, X. Zhao, K. Li, L. Yuan, *Rev. Sci. Instrum.* **2016**, 87, 074301.
- [5] H. Afsaneh, R. Mohammadi, *Talanta Open* **2022**, 5, 100092.
- [6] D. A. Ateya, J. S. Erickson, P. B. Howell, L. R. Hilliard, J. P. Golden, F. S. Ligler, *Anal. Bioanal. Chem.* **2008**, 391, 1485.
- [7] G. Zhuang, T. G. Jensen, J. P. Kutter, *Electrophoresis* **2012**, 33, 1715.
- [8] C. Mu, F. Zhang, Z. Zhang, M. Lin, X. Cao, *Sens. Actuators, B Chem.* **2011**, 151, 402.
- [9] L. Yang, W. Wang, *Microsyst. Technol.* **2019**, 25, 2241.
- [10] G. Testa, G. Persichetti, R. Bernini, *Biomed. Opt. Express* **2015**, 6, 54.
- [11] D. De Coster, H. Ottevaere, M. Vervaeke, J. Van Erps, M. Callewaert, P. Wuytens, S. H. Simpson, S. Hanna, W. De Malsche, H. Thienpont, *Opt. Express* **2015**, 23, 30991.
- [12] S. Keraman, D. Vercruyssen, T. Claes, A. Stassen, M. Mahmud Ul Hasan, P. Neutens, V. Mukund, N. Verellen, X. Rottenberg, L. Lagae, P. Van Dorpe, *ACS Photonics* **2017**, 4, 1937.
- [13] M. Rosenauer, M. J. Vellekoop, *Biomicrofluidics* **2010**, 4, 043005.
- [14] S. Balslev, A. M. Jorgensen, B. Bilenberg, K. B. Mogensen, D. Snakenborg, O. Geschke, J. P. Kutter, A. Kristensen, *Lab Chip* **2006**, 6, 213.
- [15] R. Bernini, E. De Nuccio, F. Brescia, A. Minardo, L. Zeni, P. M. Sarro, R. Palumbo, M. R. Scarfi, *Anal. Bioanal. Chem.* **2006**, 386, 1267.
- [16] M. Rosenauer, W. Buchegger, I. Finoulst, P. Verhaert, M. Vellekoop, *Microfluid. Nanofluid.* **2011**, 10, 761.
- [17] J. Guo, X. Liu, K. Kang, Y. Ai, Z. Wang, Y. Kang, *J. Light. Technol.* **2015**, 33, 3433.
- [18] J. Li, Y. Cui, Z. Wei, T. Zhou, Q. Li, *Proc. SPIE, 2021 SPIE/COS Photonics Asia*, Nantong, Jiangsu **2021**, p. 11.
- [19] M. Serhatlioglu, C. Elbuen, B. Ortac, M. E. Solmaz, Optical Fibers and Sensors for Medical Diagnostics, Treatment and Applications XVII **2017**, p. 1005801.
- [20] S. Etcheverry, A. Faridi, H. Ramachandraiah, T. Kumar, W. Margulis, F. Laurell, A. Russom, *Sci. Rep.* **2017**, 7, 1.
- [21] M. Asghari, M. Serhatlioglu, B. Ortac, M. E. Solmaz, C. Elbuen, *Sci. Rep.* **2017**, 7, 12342.
- [22] D. Schafer, E. A. Gibson, E. A. Salim, A. E. Palmer, R. Jimenez, J. Schier, *Opt. InfoBase Conf. Pap.*, **2009**, 17, 5083.
- [23] H. Yang, G. Yang, T. Zhang, D. Chen, J. Wang, J. Chen, *J. Micromech. Microeng.* **2022**, 32, 024002.
- [24] S. Joo, K. H. Kim, H. C. Kim, T. D. Chung, *Biosens. Bioelectron.* **2010**, 25, 1509.
- [25] A. V. Harish, T. Kumar, S. Etcheverry, A. Russom, W. Margulis, F. Laurell, *Opt. InfoBase Conf. Pap.*, 2020 Conference on Lasers and Electro-Optics (CLEO), San Jose, CA **2020**, Part F181, p. 2.
- [26] M. Kim, D. J. Hwang, H. Jeon, K. Hiromatsu, C. P. Grigoropoulos, *Lab Chip* **2009**, 9, 311.
- [27] T. Peng, X. Su, X. Cheng, Z. Wei, X. Su, Q. Li, *Cytometry Part A* **2021**, 99, 1107.
- [28] X. Mao, S. C. S. Lin, M. I. Lapsley, J. Shi, B. K. Juluri, T. J. Huang, *Lab Chip* **2009**, 9, 2050.
- [29] Y. Zhao, Q. Li, X. Hu, Y. Lo, *Biomicrofluidics* **2016**, 10, 064119.
- [30] I. Bernat, J. J. Gonzalez-Murillo, L. Fonseca, M. Moreno, A. Romano-Rodriguez, *Sens. Actuators, A Phys.* **2016**, 247, 629.
- [31] B. R. Watts, Z. Zhang, C. Q. Xu, X. Cao, M. Lin, *Electrophoresis* **2012**, 33, 3236.
- [32] X. Mao, J. R. Waldeisen, B. K. Juluri, T. J. Huang, *Lab Chip* **2007**, 7, 1303.
- [33] S. Hengoju, O. Shvydkiv, M. Tovar, M. Roth, M. A. Rosenbaum, *Biosens. Bioelectron.* **2022**, 200, 113910.
- [34] Y. Lyu, J. Yin, Y. Zhu, Y. Fu, A. Glidle, H. Furusho, T. Yang, H. Yin, in *Proc. SPIE, SPIE BiOS* **2021**, p. 30.
- [35] D. Barat, G. Benazzi, M. C. Mowlem, J. M. Ruano, H. Morgan, *Opt. Commun.* **2010**, 283, 1987.
- [36] S. K. Y. Tang, C. A. Stan, G. M. Whitesides, *Lab Chip* **2008**, 8, 395.
- [37] A. V. Harish, T. Kumar, A. Russom, W. Margulis, F. Laurell, *Opt. InfoBase Conf. Pap.*, 2020 Conference on Lasers and Electro-Optics (CLEO), San Jose, CA **2020**, Part F181, p. 45.
- [38] A. Mohan, P. Gupta, A. P. Nair, A. Prabhakar, T. Saiyed, *Biomicrofluidics* **2020**, 14, 054104.
- [39] R. W. Epps, K. C. Felton, C. W. Coley, M. Abolhasani, *Lab Chip* **2017**, 17, 4040.
- [40] R. W. Epps, M. S. Bowen, A. A. Volk, K. Abdel-Latif, S. Han, K. G. Reyes, A. Amassian, M. Abolhasani, *Adv. Mater.* **2020**, 32, 2001626.
- [41] A. Malekanfard, S. Beladi-Behbahani, T. R. Tzeng, H. Zhao, X. Xuan, *Anal. Chem.* **2021**, 93, 5947.
- [42] M. Kumar, S. Yadav, A. Kumar, N. N. Sharma, J. Akhtar, K. Singh, *Biosens. Bioelectron.* **2019**, 142, 111526.
- [43] D. Spencer, G. Elliott, H. Morgan, *Lab Chip* **2014**, 14, 3064.
- [44] O. Civelekoglu, N. Wang, M. Boya, T. Ozkaya-Ahmadov, R. Liu, A. F. Sarioglu, **2019 20th Int. Conf. Solid-State Sensors, Actuators Microsystems Eurosensors XXXIII, Transducers 2019 Eurosensors XXXIII**, Berlin, Germany **2019**, p. 975.
- [45] M. Helou, M. Reisbeck, S. F. Tedde, L. Richter, L. Bär, J. J. Bosch, R. H. Stauber, E. Quandt, O. Hayden, *Lab Chip* **2013**, 13, 1035.
- [46] M. Reisbeck, L. Richter, M. J. Helou, S. Arlinghaus, B. Anton, I. van Dommelen, M. Nitzsche, M. Baßler, B. Kappes, O. Friedrich, O. Hayden, *Biosens. Bioelectron.* **2018**, 109, 98.
- [47] L. Liang, X. Xuan, *Microfluid. Nanofluid.* **2012**, 13, 637.
- [48] Y. Chen, A. A. Nawaz, Y. Zhao, P. H. Huang, J. P. McCoy, S. J. Levine, L. Wang, T. J. Huang, *Lab Chip* **2014**, 14, 916.
- [49] L. Ren, S. Yang, P. Zhang, Z. Qu, Z. Mao, P. H. Huang, Y. Chen, M. Wu, L. Wang, P. Li, T. J. Huang, *Small* **2018**, 14, 1801996.
- [50] E. J. Lim, T. J. Ober, J. F. Edd, S. P. Desai, D. Neal, K. W. Bong, P. S. Doyle, G. H. McKinley, M. Toner, *Nat. Commun.* **2015**, 5, 1.
- [51] A. T. Ciftlik, M. Ettori, M. A. M. Gijs, *Small* **2013**, 9, 2764.
- [52] F. Del Giudice, *Microfluid. Nanofluid.* **2019**, 23, 1.
- [53] M. Asghari, X. Cao, B. Mateescu, D. Van Leeuwen, M. K. Aslan, S. Stavrakis, A. J. Demello, *ACS Nano* **2020**, 14, 422.
- [54] M. Serhatlioglu, Z. Isiksacan, M. Özkan, D. Tuncel, C. Elbuen, *Anal. Chem.* **2020**, 92, 6932.
- [55] A. Choudhary, D. Li, T. Renganathan, X. Xuan, S. Pushpavanam, *J. Fluid Mech.* **2020**, 898.
- [56] D. Li, X. Xuan, *Phys. Rev. Fluids* **2018**, 7, 1.
- [57] C. L. Andriamanampisoa, A. Bancaud, A. Boutonnet-Rodat, A. Didot, J. Fabre, F. Fina, F. Garlan, S. Garrigou, C. Gaudy, F. Ginot, D. Henaff, P. Laurent-Puig, A. Morin, V. Picot, L. Saia, V. Taly, P. Tomasini, A. Zaan, *Anal. Chem.* **2018**, 90, 3766.
- [58] Y. Lee, B. Kim, S. Choi, *Sens. Actuators, A Phys.* **2020**, 309, 112038.
- [59] M. Serhatlioglu, M. Asghari, M. Tahsin Guler, C. Elbuen, *Electrophoresis* **2019**, 40, 906.
- [60] D. Tang, L. Jiang, W. Tang, N. Xiang, Z. Ni, *Talanta* **2022**, 242, 123274.
- [61] C. F. Otesteanu, M. Ugrinic, G. Holzner, Y. T. Chang, C. Fassnacht, E. Guenova, S. Stavrakis, A. deMello, M. Claassen, *Cell Rep. Methods* **2021**, 1, 100094.
- [62] G. Holzner, S. Stavrakis, A. Demello, *Anal. Chem.* **2017**, 89, 11653.
- [63] G. D'Avino, G. Romeo, M. M. Villone, F. Greco, P. A. Netti, P. L. Maffettone, *Lab Chip* **2012**, 12, 1638.
- [64] C. Liu, C. Xue, X. Chen, L. Shan, Y. Tian, G. Hu, *Anal. Chem.* **2015**, 87, 6041.

- [65] P. Y. Huang, J. Feng, H. H. Hu, D. D. Joseph, *J. Fluid Mech.* **1997**, 343, 73.
- [66] M. Ugawa, S. Ota, *Small Sci.* **2022**, 2, 2100126.
- [67] J. Balsam, H. A. Bruck, A. Rasooly, *Biosens. Bioelectron.* **2015**, 64, 154.
- [68] J. Balsam, H. A. Bruck, A. Rasooly, *Analyst* **2014**, 139, 4322.
- [69] T. Jin, C. Zhang, F. Liu, X. Chen, G. Liang, F. Ren, S. Liang, C. Song, J. Shi, W. Qiu, X. Jiang, K. Li, L. Xi, *Anal. Chem.* **2021**, 93, 8134.
- [70] A. A. Elsayed, M. Erfan, Y. M. Sabry, R. Dris, J. Gaspéri, J. S. Barbier, F. Marty, F. Bouanis, S. Luo, B. T. T. Nguyen, A. Q. Liu, B. Tassin, T. Bourouina, *Sci. Rep.* **2021**, 11, 1.
- [71] K. S. Nielsen, T. B. Rungling, M. H. Dziegiel, R. Marie, K. Berg-Sørensen, in *Proc. SPIE, SPIE OPTO*, San Francisco, CA **2019**, p. 85.
- [72] Y. Deng, S. P. Davis, F. Yang, K. S. Paulsen, M. Kumar, R. Sinnott DeVaux, X. Wang, D. S. Conklin, A. Oberai, J. I. Herschkowitz, A. J. Chung, *Small* **2017**, 13, 1700705.
- [73] K. S. Lee, F. C. Pereira, M. Palatinszky, L. Behrendt, U. Alcolombri, D. Berry, M. Wagner, R. Stocker, *Nat. Protoc.* **2021**, 16, 634.
- [74] M. Iqbal, N. Zafar, H. Fessi, A. Elaissari, *Int. J. Pharm.* **2015**, 496, 173.
- [75] J. C. Saldivar, S. Hamperl, M. J. Bocek, M. Chung, T. E. Bass, F. Cisneros-Soberanis, K. Samejima, L. Xie, J. R. Paulson, W. C. Earnshaw, D. Cortez, T. Meyer, K. A. Cimprich, *Science* **2018**, 361, 806.
- [76] C. F. Nielsen, T. Zhang, M. Barisic, P. Kalitsis, D. F. Hudson, *Proc. Natl. Acad. Sci.* **2020**, 117, 12131.
- [77] A. E. C. Meijering, K. Sarlós, C. F. Nielsen, H. Witt, J. Harju, E. Kerklingh, G. H. Haasnoot, A. H. Bizard, I. Heller, C. P. Broedersz, Y. Liu, E. J. G. Peterman, I. D. Hickson, G. J. L. Wuite, *Nature* **2022**, 605, 545.
- [78] F. Del Giudice, S. Sathish, G. D'Avino, A. Q. Shen, *Anal. Chem.* **2017**, 89, 13146.
- [79] J. Doležal, J. Vrána, J. Šafář, J. Bartoš, M. Kubaláková, H. Šimková, *Funct. Integr. Genomics* **2012**, 12, 397.
- [80] H. Feng, M. Hockin, M. Capecchi, B. Gale, H. Sant, *Biomed Microfluidics* **2020**, 14, 064109.